PSFC/JA-05-42

Core Atomic Physics Studies in Alcator C-Mod

Rice, J.E., Terry, J. L., Fournier, K. B., Marmar, E. S.

Plasma Science and Fusion Center
Massachusetts Institute of Technology
Cambridge MA 02139 USA

This work was supported by the U.S. Department of Energy, Grant No. DE-FC02-99ER54512. Reproduction, translation, publication, use and disposal, in whole or in part, by or for the United States government is permitted.

Core Atomic Physics Studies in Alcator C-Mod

J. E. Rice, J. L. Terry, K. B. Fournier† and E. S. Marmar

Plasma Science and Fusion Center, MIT, Cambridge, MA 02139-4307

† *Lawrence Livermore National Laboratory, Livermore, CA 94550, USA*

Abstract

The Rydberg series ($1s^2$ – 1snp) up to n=14 of helium-like argon (Z=18) has been observed from Alcator C-Mod plasmas using a high resolution x-ray spectrometer array. High n satellites to these lines of the form $1s^2 2s$ – 1s2snp and $1s^2 2p$ – 1s2pnp with $3 \leq n \leq 12$ have been recorded. X-ray spectra of $2l$ - nl' transitions with $3 \leq n \leq 18$ in molybdenum (Z=42) and $3 \leq n \leq 12$ in krypton (Z=36) and niobium (Z=41) from charge states around neon-like have also been measured. Numerous examples of the configuration interaction, which alters the line intensities in some transitions of neon-like ions with nearly degenerate upper levels, have been observed. Accurate wavelengths of all of these transitions (± .5 mÅ) have been determined by comparison to neighboring reference lines from H- and He-like charge states. Line identifications have been made by comparison to *ab initio* atomic structure calculations, using a fully relativistic, parametric potential code. Measured line intensities have been compared with collisional radiative modeling that includes the contributions from dielectronic recombination and inner shell excitation rates, with good agreement.

I. Introduction

A wide variety of plasma diagnostic applications is available from the measurement of the relatively simple x-ray spectra of He-like ions (Ref.[1] and references therein). The n=2 and n=3 x-ray spectra from many mid- and high-Z He-like ions have been studied in magnetically confined plasmas [2-6] and in solar flares [7,8]. Always associated with x-ray emission from these two electron systems are satellite lines from lithium-like ions. Comparison of observed x-ray spectra with calculated transitions can provide tests of atomic kinetics models and structure calculations for helium- and lithium-like ions. From wavelength measurements, a systematic study of the n and Z dependence of atomic potentials may be undertaken. From the satellite line intensities, the dynamics of level population by dielectronic recombination and inner shell excitation may be addressed.

There has also been considerable interest in x-ray transitions from high Z atoms with charge states around the neon-like isosequence. X-ray lasing [9,10] has been demonstrated in neon-like ions, and a need to understand the kinetics of this system has motivated development of very precise collisional-radiative modeling tools [11]. The identifications of many x-ray lines from neon-like ions allow high resolution experimental data to be used for benchmarking multi-electron atomic structure calculations. Collisional radiative modeling of line intensities from neon-, fluorine-, sodium- and magnesium-like ionization states has demonstrated the importance of excitation-autoionization in overall charge state balance in tokamak plasmas [12]. Rates for this process, in conjunction with the latest dielectronic recombination rates [13], have led to a reassessment of the importance of molybdenum radiation for energy balance [14] in tokamak plasmas.

A brief description of the atomic structure codes and the experiment is given in the next section. In Section III are presented observations from helium-like ions and associated satellites and Section IV is devoted to neon-like ions and nearby charge states.

II. Atomic Structure Code and Experiment Description

Ab initio atomic structure calculations for the lithium-, helium- and hydrogen-like isosequences of S, Cl and Ar (Z=16, 17 and 18) with $2 \leq n \leq 14$, and the aluminum- through oxygen-like isosequences (ground states $2p^6 3s^2 3p$ to $2s^2 2p^4$, respectively) of Kr (Z=36), Mo (Z=42), Nb (Z=41), Zr (Z=40) and Pd (Z=46) have been generated using the HULLAC package. HULLAC [15,16] includes ANGLAR [17], which uses the graphical angular recoupling program NJGRAF [17] to generate fine structure levels in a jj-coupling scheme for a set of user-specified electron configurations. HULLAC then generates atomic wavefunctions using the fully relativistic, parametric potential code RELAC [15,16], which calculates the full multi-configuration, intermediate coupled level energies and radiative transition rates. RELAC also computes semi-relativistic autoionization transition rates [18] to the ground and excited levels of an adjacent ion. The CROSS [19] suite of codes in the HULLAC package uses a factorization theorem to compute the distorted wave approximation electron-impact excitation rates between all levels of each charge state mentioned above. This includes levels formed by exciting valence shell electrons as well as deeply bound inner shell electrons.

Energy levels and transition probabilities for helium- and lithium-like ions have also been calculated by using the Z-expansion method (MZ code) [20,21]. The energy matrix is constructed in an LSJ coupling scheme and relativistic corrections are included within the framework of the Breit-Pauli operator using a perturbation approach. The MZ method uses hydrogenic wavefunctions. However, the calculation energies and other characteristics by this method are greatly improved by using many-body perturbation theory to include the Coulomb interaction between electrons as well as relativistic corrections.

X-ray spectra were recorded with a von Hamos type spectrometer array, each spectrometer of which has a resolving power of 5000, a 2 cm spatial resolution and a luminosity function of 7×10^{-9} cm^2-sr, with spectra typically collected every 20 ms, and with 120 mÅ coverage. A detailed description of the x-ray and VUV

spectrometer systems was presented in Chapter VII on impurity transport and in Chapter XVIII on diagnostics. Nitrogen, argon and krypton were introduced into the plasma through a piezo-electric valve, scandium, niobium and zirconium were injected by laser blow-off and molybdenum is an intrinsic impurity.

III. He-like and Nearby Charge States

The time histories of He-like scandium emission following injection by laser blow-off were shown in Chapter VII on impurity transport. A spectrum of the central scandium x-ray emission [22] is shown in Fig.1, which is dominated by the resonance line, w ($1s^2\ ^1S_0 - 1s2p\ ^1P_1$). The forbidden line, z ($1s^2\ ^1S_0 - 1s2p\ ^3S_1$), and the intercombination lines, x ($1s^2\ ^1S_0 - 1s2p\ ^3P_2$) and y ($1s^2\ ^1S_0 - 1s2p\ ^3P_1$) are prominent. Also apparent is the n=2 dielectronic satellite k (the companion satellite j is blended with z), the n=2 inner shell satellites q and r (the related satellites s and t are blended with x and y), and the satellites with n=3 and n=4 spectators, all from lithium-like scandium. q and r can be populated by both inner shell excitation and dielectronic recombination; for typical C-Mod conditions, inner shell excitation dominates. j and k can only be populated by dielectronic recombination. On the long wavelength side above 2910 mÅ are Be-like satellites. Similar higher n transitions have been studied in argon and chlorine [22,23]. Shown in Fig.2 are x-ray spectra in the vicinity of the first three resonance lines, w ($1s^2\ ^1S_0 - 1s2p\ ^1P_1$), w_3 ($1s^2\ ^1S_0 - 1s3p\ ^1P_1$) and w_4 ($1s^2\ ^1S_0 - 1s4p\ ^1P_1$) in He-like Ar^{16+}. The n=2 spectrum is very similar to the scandium spectrum of Fig.1. For the n=3 spectrum, w_3 is dominant, the intercombination line, y_3 ($1s^2\ ^1S_0 - 1s3p\ ^3P_1$), is greatly reduced in relative magnitude and wavelength (the excitation rates and transition probabilities for x_3 and z_3 are miniscule so they are not seen) and the satellites have formed four unresolved features. The upper levels of these satellites are the same as for the unresolved satellites marked 3 in the n=2 spectrum; in this case the n=3 electron makes the transition with the n=2 electron as the spectator, whereas for the satellites marked 3 in the n=2 spectrum, the n=2 electron makes

the transition while the n=3 electron is the spectator. For the n=4 spectrum, w_4 dominates and the satellites have blended to form three unresolved groups: A_4 is related to k and j in the n=2 spectrum, B_4 to q and r, and C_4 to s and t. (See Table 6 of Ref.[24] for the wavelengths and line designations of these satellite groups.) The upper levels of these transitions are the same as for the shoulder marked 4 in the n=2 spectrum.

Shown in Fig.3 is a spectrum from argon including w_4, w_5 and w_6 from Ar^{16+}, Ly_β from Ar^{17+} and the satellite groups A_5-A_{12}, B_5-B_8 and C_5-C_7, in an overlapping 'triplet' pattern [24]. Plasma parameters for the discharge from which this spectrum was obtained were $n_{e0} = 1.3\times10^{20}/m^3$ and $T_{e0} = 1550$ eV. A synthetic spectrum is shown in the bottom frame, and the agreement is quite good. Density profiles of the individual charge states were determined from impurity transport simulations and the details are presented in Chapter VII. The transition designations, calculated wavelengths, satellite capture energies, oscillator strengths/satellite intensity factors and inner shell excitation rates (evaluated at 2000 eV) for Ar^{15+} satellites between n=4 and n=12 may be found in Tables 6-10 of Ref.[24]. The measured wavelength differences between the resonance lines, w_n, and the satellite groups A_n, B_n and C_n, as a function of n for argon are shown in Fig.4. Also shown are the theoretical values (curves), from the calculated wavelengths of Tables 6-10 of Ref.[24]; the solid lines are from the MZ wavelengths and the dotted lines represent the wavelengths from RELAC. The agreement between the observed wavelengths and those calculated from MZ is excellent.

Spectra near the Ar^{16+} Rydberg series limit [23,24] are shown in Fig.5. The top spectrum was taken along the central chord of a plasma with $n_{e0} = 0.9\times10^{20}/m^3$ and $T_{e0} = 2600$ eV. The resonance lines from w_6 to w_{14} are clearly resolved, and there is a region of enhanced brightness from w_{15} up to the series limit at 3008.8 mÅ, presumably due to unresolved lines. Along this chord, most of the line emission is from the plasma center where electron impact excitation is the dominant mechanism for populating the upper levels. Ar^{17+} Ly_γ near 2987.4 mÅ is also prominent. The corresponding spectrum from an identical plasma, but taken along a chord viewing

through r/a = 0.67 (away from the lower X-point), where the electron temperature was 1100 eV and the electron density was $0.8\times10^{20}/m^3$, is shown in the middle frame of Fig.5. The lines are greatly reduced in intensity and the widths are very narrow due to the lower ion temperature. The intensities of w_9 and w_{10} are enhanced relative to the trend of decreasing intensity with increasing n number, which is due to population by charge exchange recombination with intrinsic neutral deuterium in the ground state, near the plasma edge [25,23]. Emission from the very high n levels (n > 25) is also visible just on the long wavelength side of series limit. Along this chord, however, the lines w_{11} through w_{14} are not visible. The continuum at wavelengths shorter than the limit is greater than the continuum level between the resonance lines, and is due to radiative recombination. The spectrum shown in the bottom frame is from a somewhat similar plasma, from a chord viewing through r/a = 0.62, but 19.7 cm below the mid-plane, for a lower X-point discharge. In this case w_{10} is enhanced relative to the other w_n lines (due to population by charge exchange with intrinsic neutral deuterium in the ground state) and the feature on the long wavelength side of the limit is now dominant. This feature is from n numbers between 30 and 40, and is due to charge exchange between hydrogen-like argon and intrinsic neutral deuterium in the n=3 and n=4 excited states.

There are some interesting and subtle manifestations of the edge impurity transport coefficient profiles in the intensities of impurity emission from the plasma periphery (see Chapter VII on impurity transport, Sections III and VI). The slow *edge* impurity transport of L-mode enables the inner shell satellites of lithium-like nitrogen to dominate the resonance line of helium-like N^{5+} in the extreme edge of the plasma [26]. For most Alcator C-Mod operating conditions for viewing chords out to r/a = 0.8, the N^{5+} spectrum near 29 Å is comprised of only two lines, the resonance line, w ($1s^2\ ^1S_0$ - $1s2p\ ^1P_1$ at 28.787 Å) and the intercombination line, y ($1s^2\ ^1S_0$ - $1s2p\ ^3P_1$ at 29.084 Å). At the extreme plasma periphery ($r/a \geq 0.9$), the inner shell satellites q ($1s^22s\ ^2S_{1/2}$ - $1s2s2p\ ^2P_{3/2}$ at 29.441 Å), r ($1s^22s\ ^2S_{1/2}$ - $1s2s2p\ ^2P_{1/2}$ at 29.443 Å), s ($1s^22s\ ^2S_{1/2}$ - $1s2s2p\ ^2P_{3/2}$ at 29.155 Å) and t ($1s^22s\ ^2S_{1/2}$ - $1s2s2p\ ^2P_{1/2}$ at 29.155 Å) are also visible, as seen in Fig.6. The lines y, s

and t form an unresolved composite at 29.1 Å and q and r comprise an unresolved feature at 29.5 Å. In the top frame of Fig.6 is a spectrum obtained along a viewing chord at 20.5 cm (r/a = .91) during the H-mode period of a 5.3 T discharge with nitrogen injection, and the resonance line still dominates the spectrum. In the bottom frame of the figure is a spectrum obtained from the same viewing chord after the same plasma has reentered L-mode, and the satellites q and r have become the strongest lines. Also shown in the figure by the smooth dash-dot curves are synthetic spectra whose line intensities are generated (by the method outlined in Chapter VII on impurity transport) from calculated brightness profiles and whose wavelengths are taken from Ref.[27]. The relative intensities of the calculated lines are in good agreement with the observations, while there is a slight shift (.05 Å) between the measured and calculated wavelengths for q and r. The brightnesses were determined from the calculated emissivity for the six lines, which are shown in Fig.7. In the top frame are the profiles near the edge generated using the appropriate H-mode transport coefficients, and in the bottom frame are shown the profiles for the L-mode case (see Chapter VII on impurity transport). Shown by the thin lines are the helium- and lithium-like density profiles. In both cases the satellite lines are emitted in a thin shell around 20.5 cm, in spite of the fact that the H- and L-mode electron temperature profiles are different. In the L-mode case the satellites are the dominant lines at 20.5 cm because there is no inward convection to sweep the lithium-like nitrogen quickly through the region where the electron temperature is appropriate for the excitation of these lines, before ionization occurs.

IV. Ne-like and Nearby Charge States

Intense x-ray emission also arises from ions of the next closed shell, neon-like. The brightest n=3 to 2 transitions in neon-like ionization states have been studied extensively in a variety of plasmas [28-30]. Higher n transitions have been observed in Alcator C-Mod plasmas [12,31-33]. Shown in Fig.8 are Δn=2 spectra, with the upper levels in n=4, for the neon-like ions Mo^{32+} and Kr^{26+}. The 4D line ($2p_{\frac{3}{2}}$ -

$4d_{\frac{5}{2}}$ or $2p_+ - 4d_+$) dominates the molybdenum spectrum, and similar transitions from the Na- and F-like charge states are prominent. (See Tables in Ref.[31] for wavelengths and transition designations.) Complete spatial brightness profiles [12] have been obtained by scanning the spectrometer systems on a shot by shot basis during a sequence of similar discharges. Radial brightness profiles of the five most intense molybdenum x-ray lines [3614.9 (F-like), 3626.1 (Ne-like 4C), 3671.0 (Na-like), 3739.8 (Ne-like 4D) and 3785.7 mÅ(Na-like)], obtained during several similar plasmas, with a central electron density of 1.6 x $10^{20}m^{-3}$ and a central electron temperature of 2200 eV, are shown in Fig.9. The Mo^{32+} profiles (×s and plus signs) dominate over the inner half of the plasma. The Mo^{31+} profile shapes (squares and diamonds) are broader, and the Mo^{33+} profile (asterisks) is narrower than the Mo^{32+} profiles. Also shown in the figure are the calculated brightness profiles (curves) for the five lines, and the agreement is excellent. All of the profile shapes and the relative intensities are well matched by the calculations. This agreement indicates that the combination of the electron temperature and density profiles, the transport coefficients and the excitation, ionization and recombination rates is well characterized for these ionization states over the inner 10 cm. In this region the electron temperature and density profiles and impurity transport coefficients are independently measured and well known. Thus the match in Fig.9 (top) is taken as evidence in support of the charge state profiles shown in Fig.10a. The brightness profiles calculated from the charge state profiles of Fig. 10b (i.e. those without excitation-autoionization) are shown in the bottom of Fig.9, along with the measured profiles. Both the profile shapes and the relative intensities do not represent the data, demonstrating the importance of excitation-autoionization in the overall ionization rate and the sensitivity of this comparison.

The charge state distribution for molybdenum were calculated from the MIST [34] impurity transport code, incorporating the new excitation-autoionization (EA) and dielectronic recombination (DR) rates from Ref.[13], using measured electron temperature and density profiles, and impurity transport coefficients (see Chapter VII). Shown in Fig.10a are the fractional abundances of molybdenum charge states

as a function of minor radius in the plasma, calculated using the new ionization and recombination rates. The new ionization rate coefficients include contributions from direct ionization, calculated using the formulas found in Ref.[35], and for EA as found in Ref.[13]. Ne-like Mo^{32+} is the dominant state over most of the interior plasma and the neighboring charge states are all present in appreciable quantities. The Na-like Mo^{31+} profile peaks around 7 cm and the Cl-like Mo^{25+} profile peaks at 13.8 cm. Shown for comparison in Fig.10b are the charge state profiles calculated using older ionization [36] rates with no EA and recombination [37,38] rates using a semi-empirical form for DR. There is a striking difference in the core charge state distribution, largely due to the effects of the more accurate calculation of direct collisional ionization and inclusion of excitation-autoionization. The central fractional abundance of Mo^{32+} is a factor of 3 lower in Fig.10b than in Fig.10a, and the profile shapes have all changed. The Mo^{31+} state is now centrally peaked and the peak in Mo^{25+} is at 12.8 cm. These differences can strongly affect conclusions about molybdenum densities in the plasma from various charge states.

Shown in the bottom of Fig.8 are the 4D ($2p_+ - 4d_+$) and 4C ($2p_- - 4d_-$) lines of Kr^{26+} at 5396.4 and 5278.7 mÅ, respectively, along with neighboring satellites and the neon-like 4F ($2p_- - 4s_+$) line at 5407.3 mÅ. Central parameters for the plasma from which this spectrum was obtained were $T_e = 1150$ eV and $n_e = 1.6\times10^{20}/m^3$. Also shown is a synthetic spectrum, which is in good agreement with the observations, although there is a ~ -10 mÅ shift of the calculated wavelength for the magnesium-like $2p_- - 4d_-$ transition at 5436.6 mÅ. The 4F transition at 5407.3 mÅ is readily noticeable, having about 10% of the intensity of the 4D transition; the 4F line in Mo^{32+} at 3705.6 mÅ was too weak to be reported in Ref.[31], but can be seen in the top of Fig.8, with about 1% of the intensity of 4D. The reason the 4F line is so intense in Kr^{26+} is because of its close proximity to the 4D line; the upper levels are separated by only 4.6 eV, and significant configuration interaction results that transfers strength from 4D to 4F [33]. The energy level diagrams for n = 4 transitions in neon-like molybdenum and krypton are shown in Fig.11. As can be seen, the upper levels for the 4D and 4F transitions in Kr^{26+}

are very close, within 4.6 eV, while in Mo^{32+} these levels are 31 eV apart, too far away for any significant configuration interaction. This phenomenon has been seen between the 7D and 6C levels in Mo^{32+} [12,31-33], but in contrast here, the *shorter* wavelength line is the beneficiary of the enhanced intensity. This effect is summarized in Fig.12, where spectra including the 7D and 6C transitions are shown for Mo, Nb, Zr and Kr. For Kr and Zr, where the lines are well separated in energy and there is no configuration interaction (CI), the intensity ratio 7D/6C is about 2/1. In the case of Mo, where the upper levels are only separated by 3.5 eV and where the CI is strong, 7D is greatly enhanced at the expense of 6C. The brightness ratios for these lines as a function of level separation for various row 5 metals are shown in Fig.13. The agreement between experiment and theory is quite good. This effect is predicted to change sign in Tc or in Ru and observations of these elements would be an important test of the theory. It is noteworthy that in the case of the 2p − nd configuration interaction, as in Figs.12 and 13, the 'beneficiary' (7D) of the enhanced intensity is on the short wavelength side (higher energy side) whereas in the case of 2p − ns level enhancement, Fig.8, the 'beneficiary' (4F) is on the long wavelength side (lower energy side) of the 'donor' transition.

Moving to even higher n transitions, shown in Fig.14 is a spectrum from 2.9 to 3.0 Å, obtained from a series of identical discharges with n_{e0} = 1.7 x $10^{20}/m^3$ and T_{e0} = 2300 eV. The nD ($2p_{\frac{3}{2}}$ - $nd_{\frac{5}{2}}$) series (red) up to n = 18 and the nC ($2p_{\frac{1}{2}}$ - $nd_{\frac{3}{2}}$) series with $8 \leq n \leq 12$ (green) are clearly resolvable. Above n = 18, the lines of the nD series blend together, up to the series limit at 2914.78 mÅ. Also shown are two Ar^{17+} lines used for the wavelength calibration, and a strong F-like Mo^{33+} line at 2929.9 mÅ. At the bottom of the figure are calculated lines from Mo^{32+} (solid), Mo^{33+} (dashed) and Ar^{17+} (dotted). Also visible are the Mo^{32+} 2s-6p and 2s-7p doublets at 2983 and 2903 mÅ, respectively.

V. Discussion and Conclusions

The high n Rydberg series of helium-like Ar^{16+} has been resolved up to n=14 in

Alcator C-Mod plasmas, and the associated lithium-like satellites up to n=12 have also been seen. Comparison of observed satellite wavelengths has been made with calculations from two different atomic structure codes, RELAC and MZ, and there is good agreement in general. The calculated intensities of the satellite groups relative to the resonance lines are also in good agreement with the observed line brightnesses, verifying the dielectronic recombination and inner shell excitation rates.

High n transitions (up to n=18) in neon-like molybdenum and (up to n=12) in neon-like krypton have also been recorded. Radial profiles of 2p-4d transitions of Na-, Ne- and F-like molybdenum demonstrate the importance of excitation-autoionization in overall charge state balance. Configuration interaction effects in certain neon-like line intensities have been observed, for transitions with nearly degenerate upper levels; comparison of observed line intensities with those calculated from RELAC is excellent.

VI. Acknowledgements

The authors thank U. Safronova for atomic structure calculations, A. Hubbard for electron temperature measurements, J. Irby for electron density measurements and the Alcator C-Mod operations and ICRF groups for expert running of the tokamak. Work supported at MIT by DoE Contract No. DE-FC02-99ER54512.

References

[1] J.E.Rice et al., Fusion Eng. Des. **34** and **35** (1997) 159.

[2] TFR Group, J. Dubau and M. L. Loulergue, J. Phys. B: At. Mol. Phys. **15** (1981) 1007.

[3] M. L. Apicella, R. Bartiromo, F. Bombarda and R. Giannella, Phys. Lett. **98A** (1983) 174.

[4] M. Bitter, K. W. Hill, M. Zarnstorff, S. von Goeler, R. Hulse, K. M. Young, L. C. Johnson, N. R. Sauthoff, S. Secnic, M. Tavernier, F. Bely-Dubau, P. Faucher, M. Cornille and J. Dabau, Phys. Rev. A **32** (1985) 3011.

[5] M. Bitter et al., Phys. Rev. Lett. **91** (2003) 265001.

[6] Shigeru Morita and Motoshi Goto, Rev. Sci. Instrum. **74** (2003) 2375.

[7] C. P. Bhalla, A. N. Gabriel and L. P. Presnyakov, Mon. Not. R. Astron. Soc. **172** (1975) 359.

[8] P. Beiersdörfer, R. Philips, V. I. Jacobs, K. W. Hill, M. Bitter, S. von Goeler and S. M. Kahn, Astrophys. J. **409** (1993) 846.

[9] M.D. Rosen et al., Phys. Rev. Lett. **54** (1985) 106.

[10] D.L. Matthews et al., Phys. Rev. Lett. **54** (1985) 110.

[11] A.L. Osterheld et al., J. Quant. Spectrosc. Radiat. Transfer **51** No. 1/2, (1994) 263.

[12] J.E. Rice et al., J. Phys. B **29** (1996) 2191.

[13] K.B. Fournier et al., Phys. Rev. A **54** (1996) 3870.

[14] K.B. Fournier, D. Pacella, M.J. May, M. Finkenthal and W.H. Goldstein, Nucl. Fusion **37** (1997) 825. (corrigendum Nucl. Fusion **38** (1998) 639.)

[15] M.Klapisch, Comput. Phys. Commun. **2** (1971) 239.

[16] M.Klapisch, J.L.Schwob, B.S.Fraenkel and J.Oreg, J. Opt. Soc. Am. **67** (1977) 148.

[17] Bar-Shalom, A. and Klapisch, M., Computer Phys. Comm. **50** (1988) 375.

[18] Oreg, J., Goldstein, W.H., Klapisch, M. and Bar-Shalom, A., Phys. Rev. A **44** (1991) 1750.

[19] Bar-Shalom, A., Klapisch, M. and Oreg, J., Phys. Rev. A **38** (1988) 1773.

[20] L.A.Vainshtein and U.I.Safronova, Physica Scripta **31** (1985) 519.

[21] U.I.Safronova and J.Nilsen, J. Quant. Spectrosc. Radiat. Transfer **51** (1994) 853.

[22] J.E.Rice et al., J. Phys. B **28** (1995) 893.

[23] J.E.Rice et al., Phys. Rev. A **35** (1987) 3033.

[24] J.E. Rice et al., New J. Phys. **1** (1999) 19.

[25] J.E.Rice et al., Phys. Rev. Lett. **56** (1986) 50.

[26] J.E.Rice et al., Phys. Plasmas **4** (1997) 1605.

[27] L. A. Vainshtein and U. I. Safronova, At. Data Nucl. Data Tables **21** (1978) 49.

[28] P. G. Burkhalter et al., Phys. Rev. A **18** (1978) 718.

[29] E. Källne, J. Källne and R.D. Cowan, Phys. Rev. A **27** (1983) 2682.

[30] S. Ya. Khakhalin et al., Phys. Scripta **50** (1994) 106.

[31] J.E. Rice et al., Phys Rev A **51** (1995) 3551.

[32] J.E. Rice et al., Phys Rev A **53** (1996) 3953.

[33] J.E. Rice et al., J. Phys. B **33** (2000) 5435.

[34] R. A. Hulse, Nucl. Tech./Fus. **3** (1983) 259.

[35] D. Sampson and L. Golden, Ap. J. **170** (1971) 169.

[36] D.E. Post, R.V. Jensen, C.B. Tarter, W.H. Grasberger, and W.A. Lokke, At. Data Nucl. Data Tables **20** (1977) 397.

[37] A.Burgess, Ap. J. **139** (1964) 776.

[38] A.Burgess, Ap. J. **141** (1965) 1588.

Figure Captions

Fig. 1 The Δn=1 spectrum of helium-like Sc^{19+} and satellites.

Fig. 2 X-ray spectra in the vicinity of the n=2, 3 and 4 resonance lines, w (top), w_3 (middle) and w_4 (bottom), showing the n=2 dielectronic satellites k and j, and n=2 inner shell satellites q, r, s and t, along with the related higher n satellite groups A_n, B_n and C_n. The A_5 dielectronic satellite group associated with w_5 is also visible, along with two high n neon-like Mo^{32+} lines (see next section).

Fig. 3 The linear scale x-ray spectrum of helium-like Ar^{16+} w_4, w_5 and w_6, with satellites, and hydrogen-like Ar^{17+} Ly_β, is shown in the top frame. In the bottom frame are the log scale observed and computed spectra for Ar^{16+}, Ar^{17+} and Ar^{15+}.

Fig. 4 The difference between the satellite wavelengths and the resonance line wavelengths in Ar^{16+} as a function of n, for the three satellite groups, along with the theoretical wavelengths. The measured values for A_n, B_n and C_n are depicted as asterisks, triangles and dots, respectively. The satellite group A'_3 is shown as the $\times$. The theoretical wavelength differences are shown by the curves, with the calculated value for A'_3 (from RELAC) given by the dot. The solid lines are from MZ, while the dotted lines are from RELAC.

Fig. 5 Spectra near the Ar^{16+} series limit. In the top frame is the spectrum from a central chord view, in the middle frame is a spectrum from an identical plasma with a view 18.5 cm above the midplane (r/a=.67) and in the bottom frame is a spectrum from a similar plasma with a view 19.7 cm below the midplane (r/a=.62). The ionization limit is shown as the vertical line. The lower spectrum was cut off below 2990 mÅ.

Fig. 6 Helium-like nitrogen spectra including inner shell satellite lines during the H-mode (top) and L-mode (bottom) phase of a plasma with nitrogen injection,

obtained from a chord viewing the edge plasma at 20.5 cm (r/a = .91). Shown by the smooth dash-dot curves are synthetic spectra.

Fig. 7 Calculated nitrogen emissivity profiles for H-mode (top) and L-mode (bottom) plasmas. The resonance and intercombination lines (w and y) of helium-like nitrogen are solid, and the inner shell lithium-like lines (q, r, s and t) are shown as dash-dot lines. The helium-like and lithium-like *densities* (same scale but in units of cm^{-3}) are shown by the thin lines.

Fig. 8 Linear and log spectra in the vicinity of 4D in Mo^{32+} are shown in the top frame. Also shown is the synthetic collisional radiative synthetic spectrum, with Ne-like lines shown as solid lines, Na-like transitions depicted by the dotted lines, the Mg-like transition shown as the dashed line and F-like transitions shown by dash-dot lines. The spectrum of the Kr^{26+} 4C, 4D and 4F transitions, with Na- and Mg-like $2p_- - 4d_-$ satellites is shown in the bottom frame. Also shown is a synthetic spectrum.

Fig. 9 Measured (symbols) and calculated (lines) x-ray brightness profiles using the charge state density profiles of Fig.10a are shown in the top frame. The solid lines are from Ne-like molybdenum, dotted lines from Na-like and dashed lines from F-like. Calculated brightness profiles for the ionization balance of Fig.10b are shown in the bottom.

Fig. 10 Calculated molybdenum charge state radial profiles a.) with excitation-autoionization (EA) and new dielectronic recombination (DR) rates and b.) with old DR rates and without EA. Solid lines are for even charge states and dashed lines are for odd.

Fig. 11 The n=4 energy level diagrams for Mo^{32+} (top) and Kr^{26+} (bottom) with the left ordinates expressed in the transition (to the ground state) wavelengths and the right ordinates in eV. Upper levels for s are on the left and for d are on the

right. Measured transition wavelengths (to the ground state) are given for each of the upper levels.

Fig. 12 Spectra in the vicinity of 7D and 6C from (top to bottom) neon-like Mo, Nb, Zr and Kr. Synthetic spectra for 7D and 6C are shown as solid lines, along with Na-like (dotted) and F-like (dash-dot) satellites.

Fig. 13 The intensity ratios of Ne-like 7D to 6C transitions as a function of energy level separation. Calculations are shown as dots, measurements are represented as asterisks.

Fig. 14 Transitions in Mo^{32+} near the nD series limit, including the nC series (green) with $8 \leq n \leq 13$ and the nD series (red) with $11 \leq n \leq 18$. Theoretical lines for Mo^{32+} (solid red, green and purple), Mo^{33+} (black dashed), and Ar^{17+} (purple dotted) are shown at the bottom.

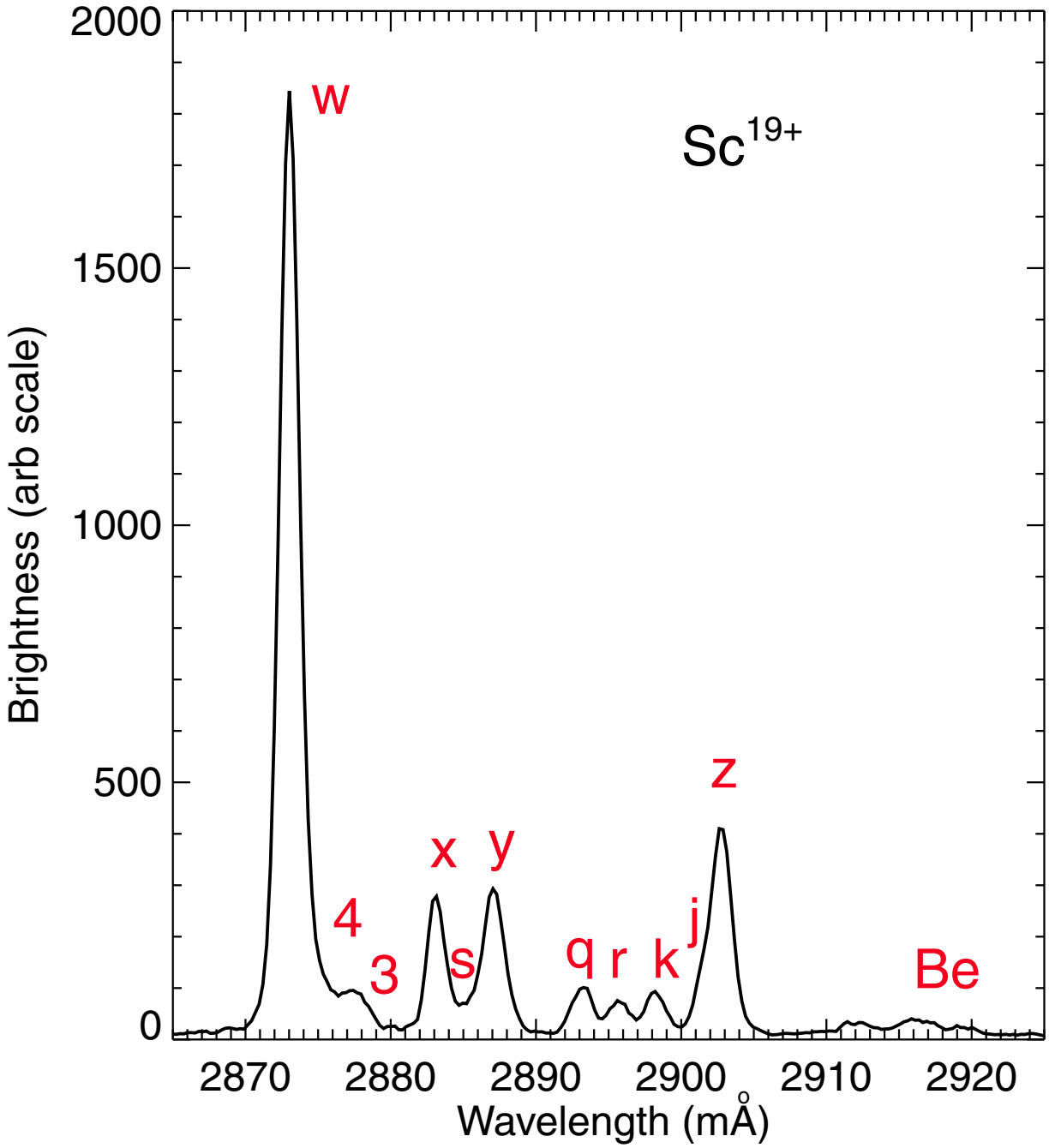
2000
1500
1000
500
0
Brightness (arb scale)
w
Sc19+
z
x
y
4
3
s
q
r
k
j
Be
2870
2880
2890
2900
2910
2920
Wavelength (mÅ)

Figure 1

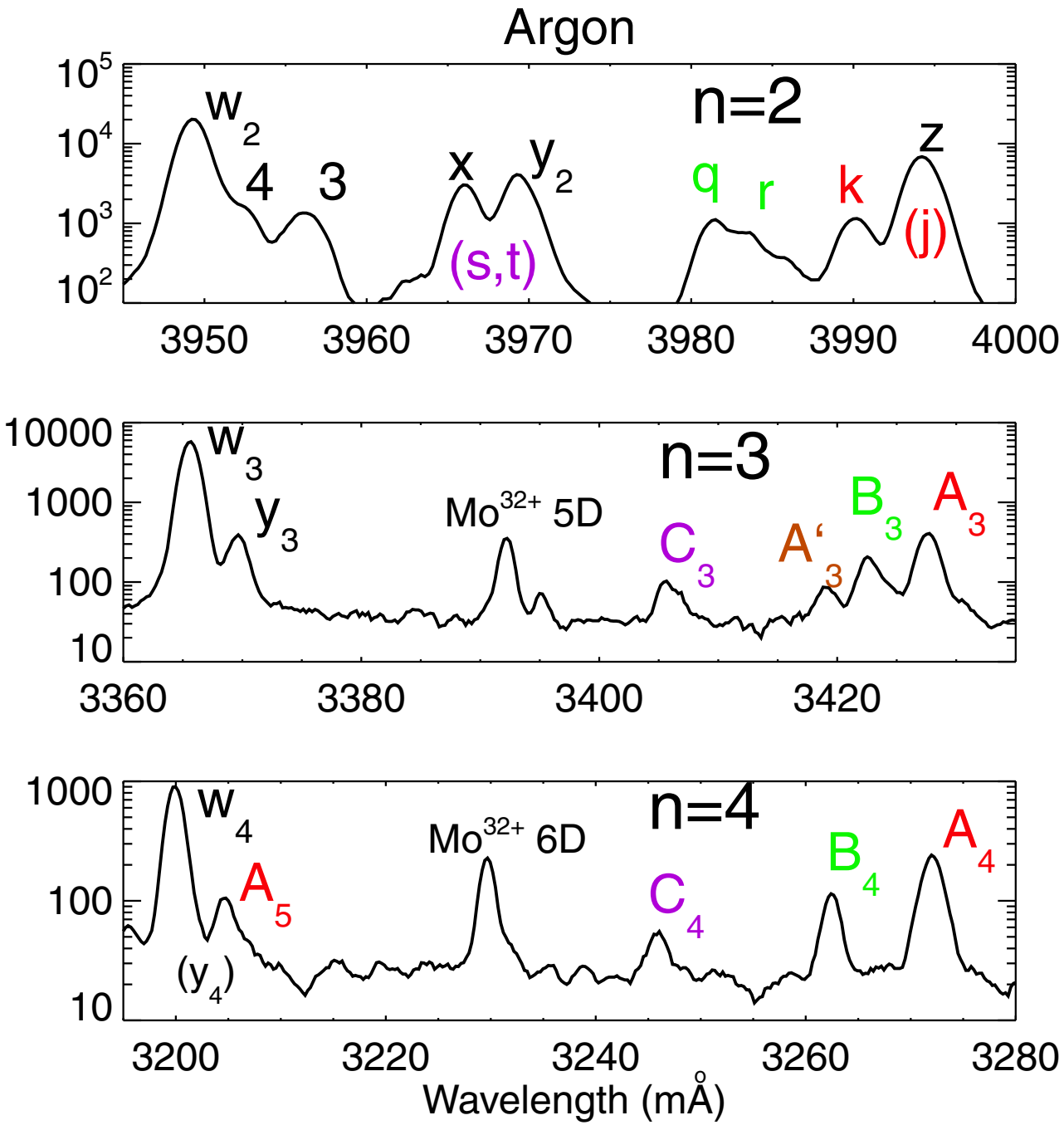
Argon
n=2
w2
4
3
x
y2
(s,t)
q
r
k
z
(j)
n=3
w3
y3
Mo32+ 5D
C3
A'3
B3
A3
n=4
w4
A5
(y4)
Mo32+ 6D
C4
B4
A4
Wavelength (mÅ)

Figure 2

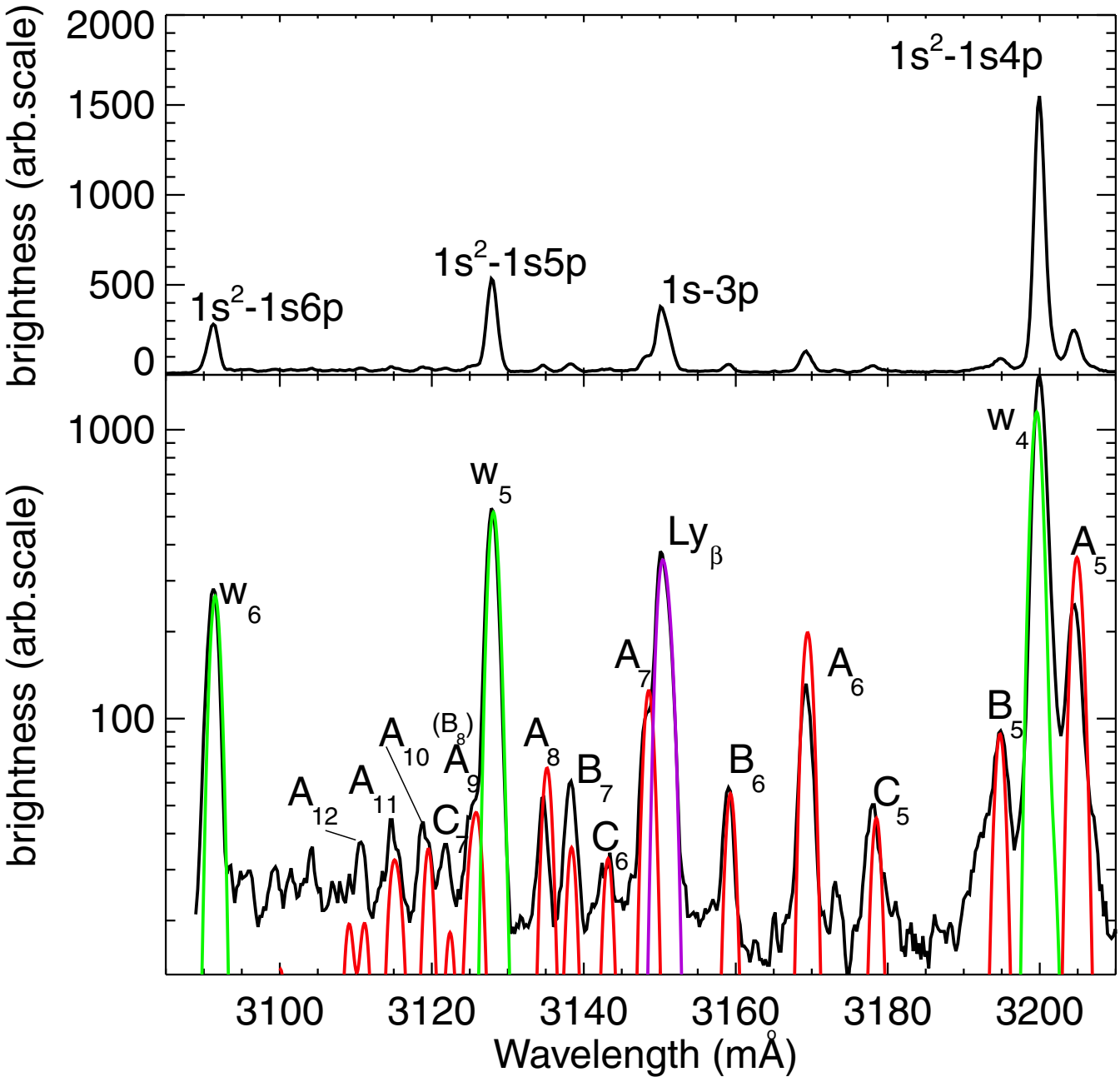
brightness (arb.scale)
2000
1500
1000
500
0
1s²-1s6p
1s²-1s5p
1s-3p
1s²-1s4p
brightness (arb.scale)
1000
100
w6
A12
A11
A10
(B8)
A9
C7
w5
A8
B7
C6
A7
Lyβ
B6
A6
C5
w4
B5
A5
3100
3120
3140
3160
3180
3200
Wavelength (mÅ)

Figure 3

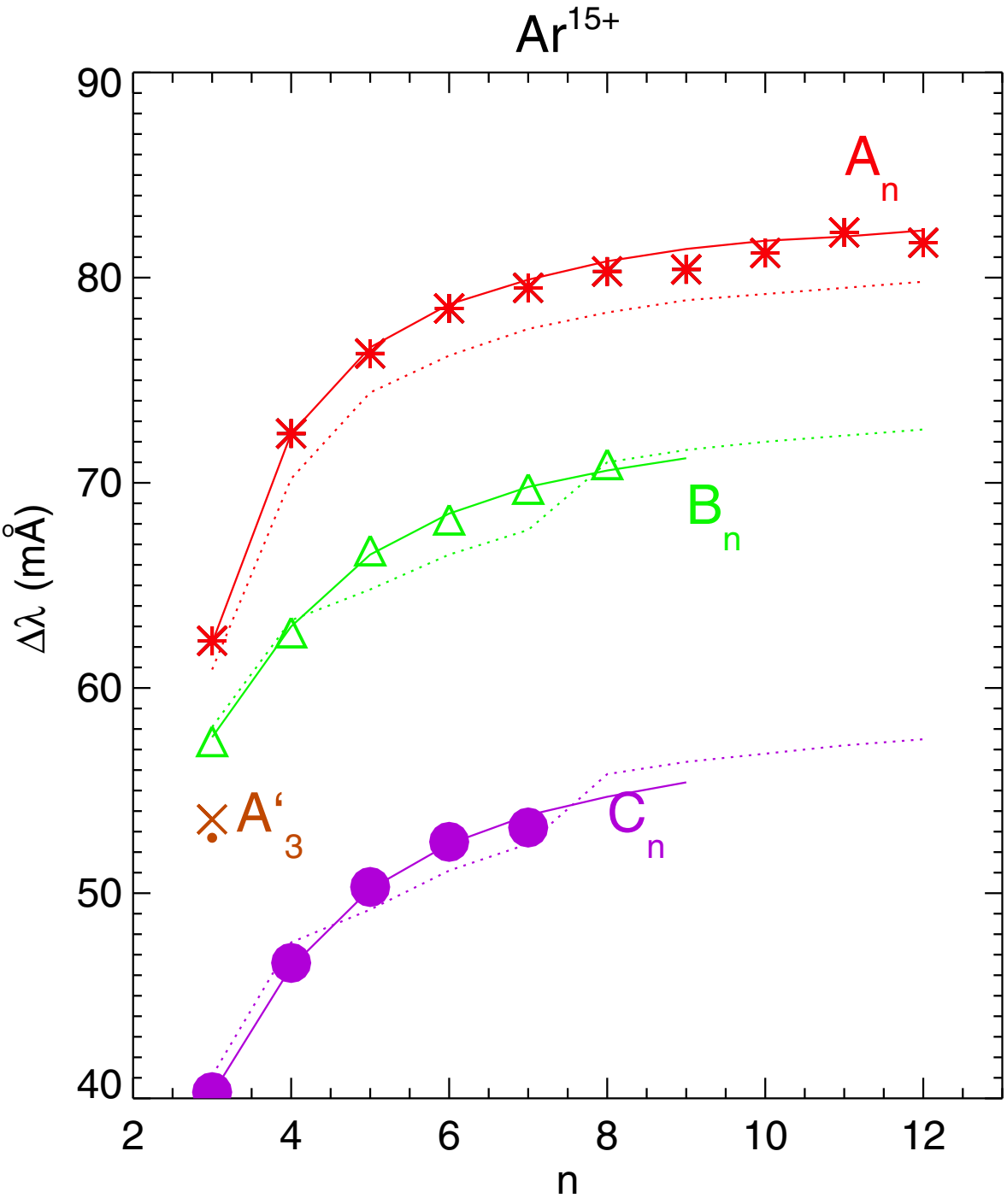

Figure 4

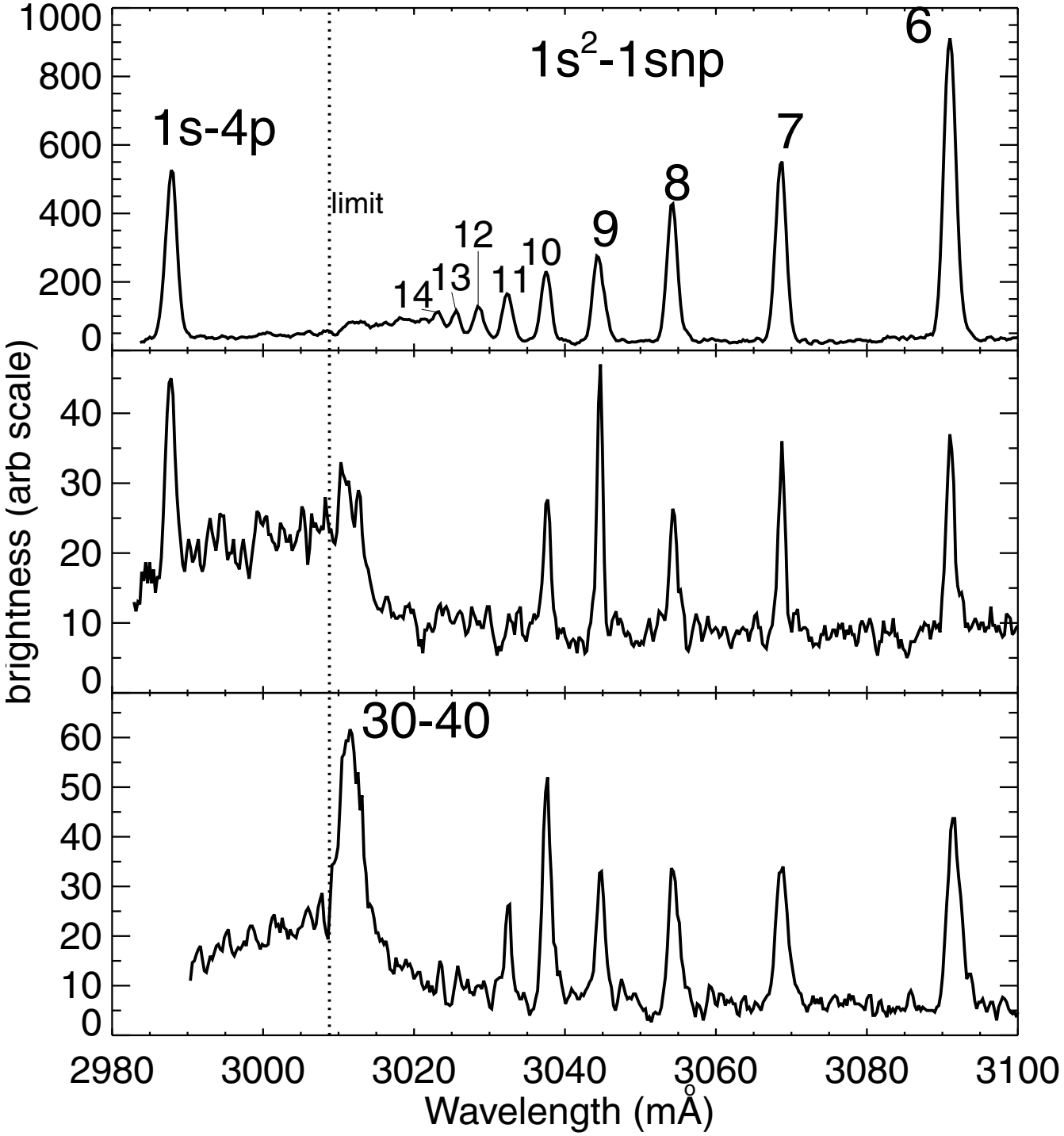
1s-4p
limit
1s²-1snp
6
7
8
9
10
11
12
13
14
30-40
brightness (arb scale)
Wavelength (mÅ)
2980
3000
3020
3040
3060
3080
3100

Figure 5

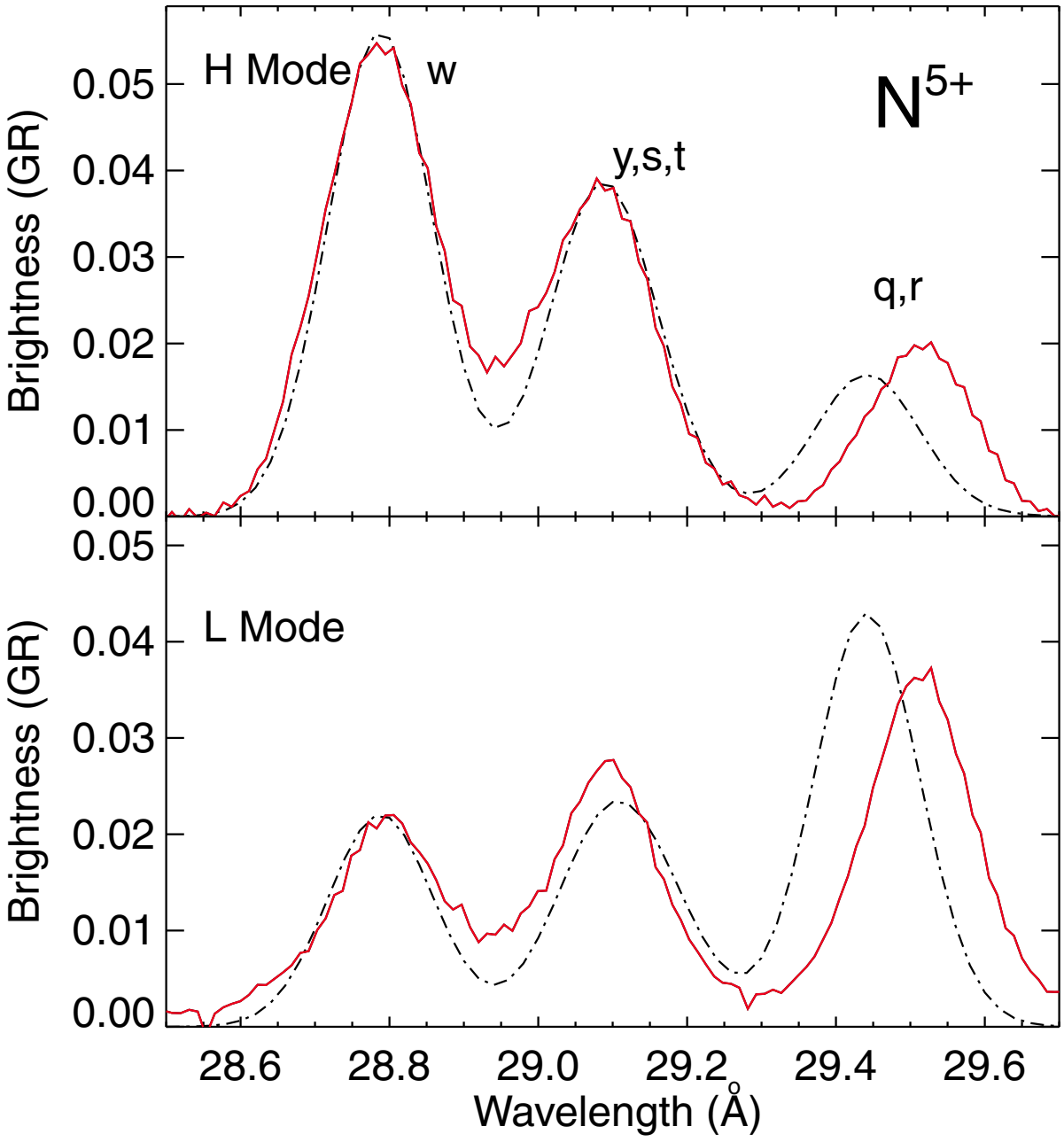
H Mode
w
y,s,t
q,r
N5+
L Mode
Brightness (GR)
0.05
0.04
0.03
0.02
0.01
0.00
28.6
28.8
29.0
29.2
29.4
29.6
Wavelength (Å)

Figure 6

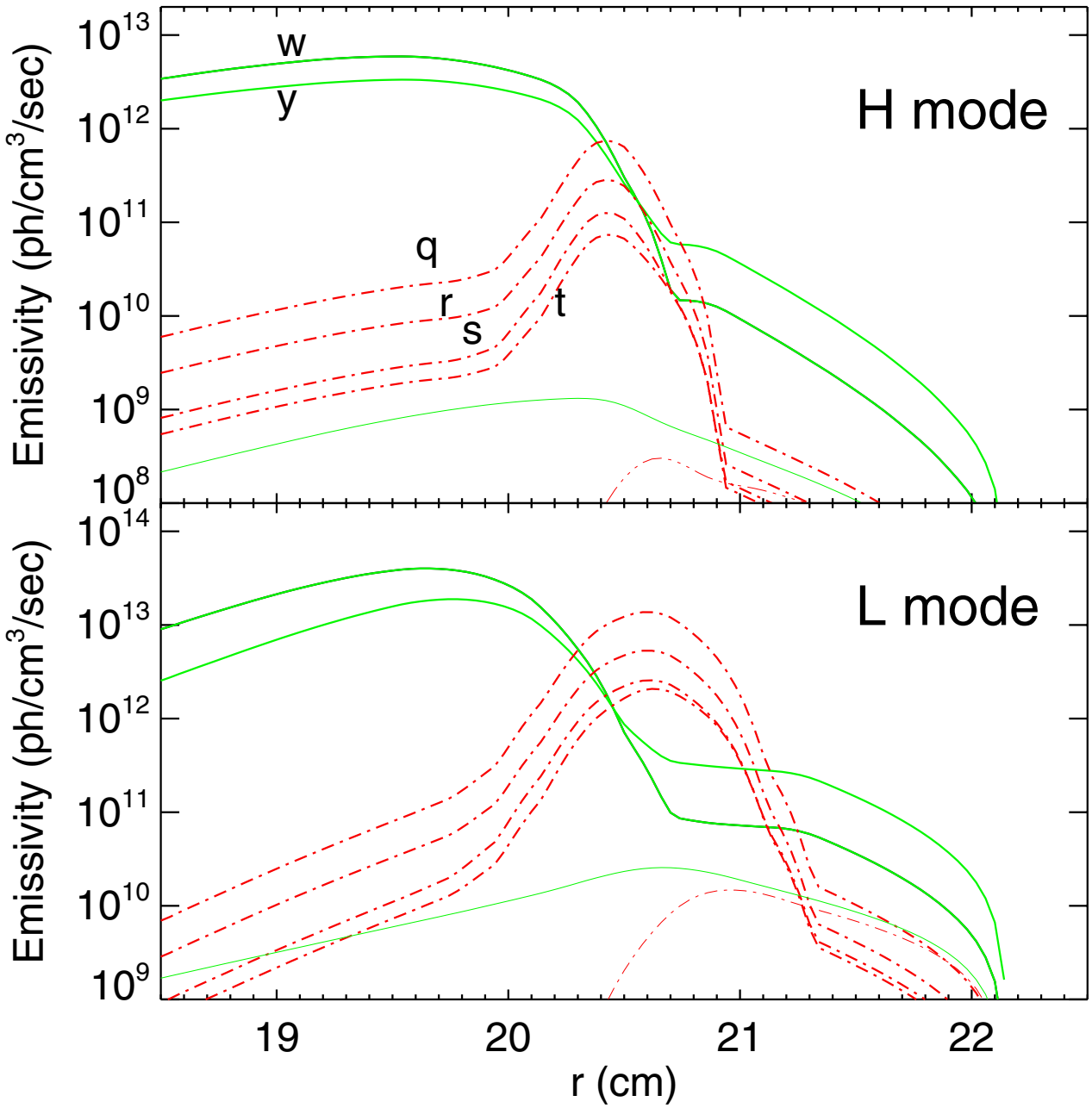
H mode
L mode
w
y
q
r
s
t
Emissivity (ph/cm^3/sec)
Emissivity (ph/cm^3/sec)
10^{13}
10^{12}
10^{11}
10^{10}
10^{9}
10^{8}
10^{14}
10^{13}
10^{12}
10^{11}
10^{10}
10^{9}
19
20
21
22
r (cm)

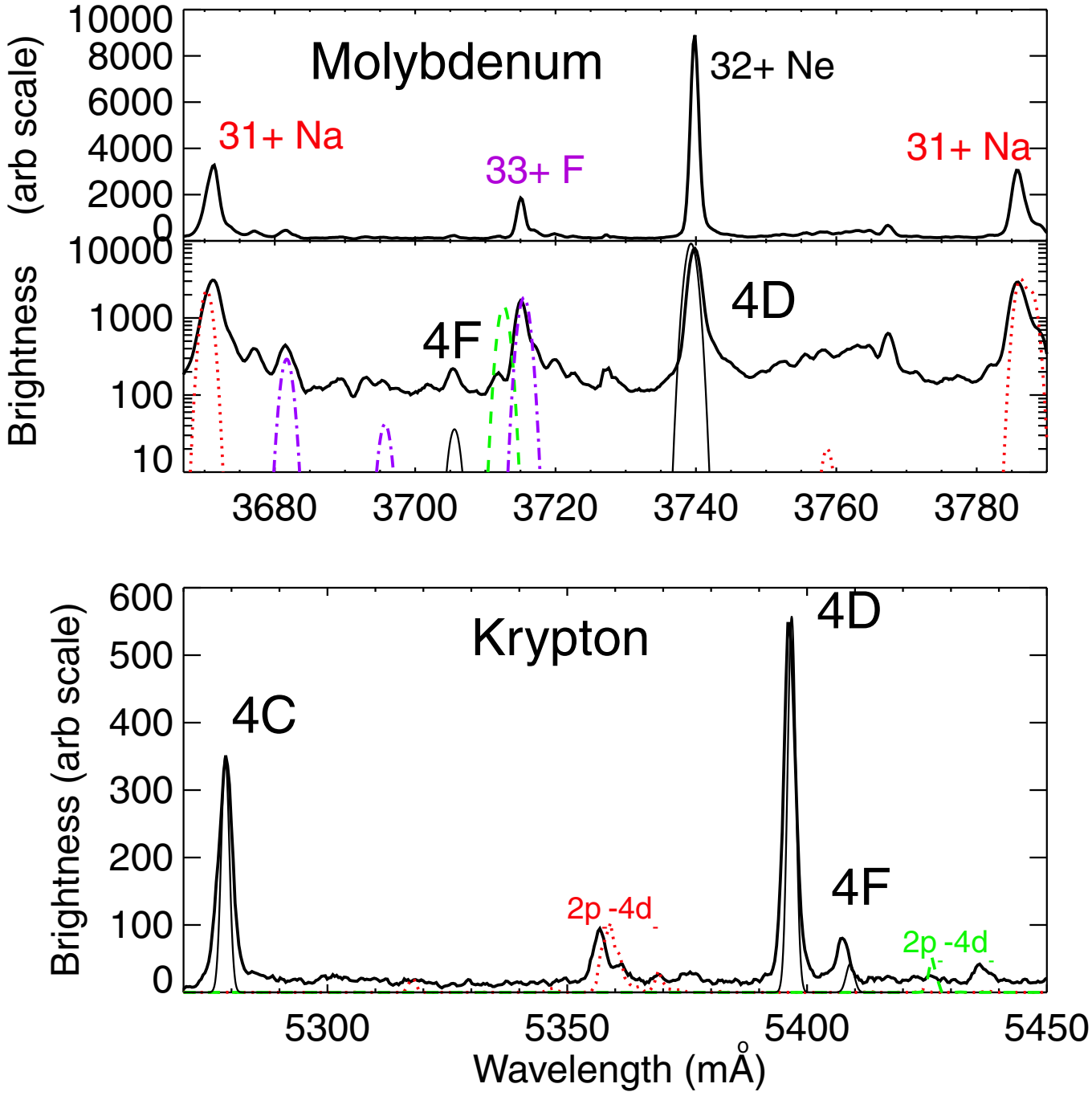
Molybdenum
32+ Ne
31+ Na
33+ F
31+ Na
4F
4D
Brightness (arb scale)
10000
8000
6000
4000
2000
0
1000
100
10
3680
3700
3720
3740
3760
3780
Krypton
4D
4C
4F
2p -4d
2p -4d
Brightness (arb scale)
600
500
400
300
200
100
0
5300
5350
5400
5450
Wavelength (mÅ)

Figure 8

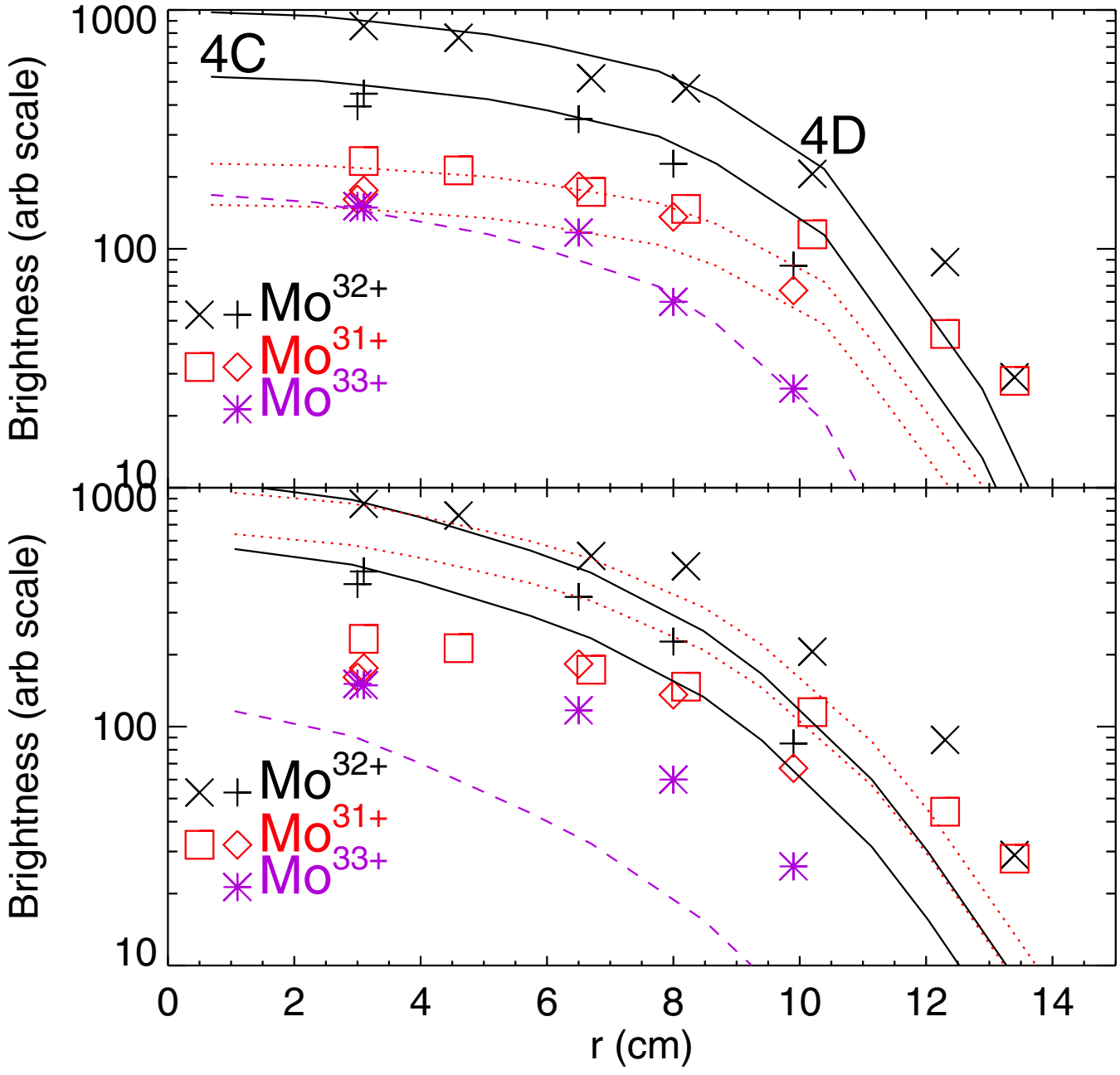
4C
4D
Mo32+
Mo31+
Mo33+
Brightness (arb scale)
1000
100
10
0
2
4
6
8
10
12
14
r (cm)

Figure 9

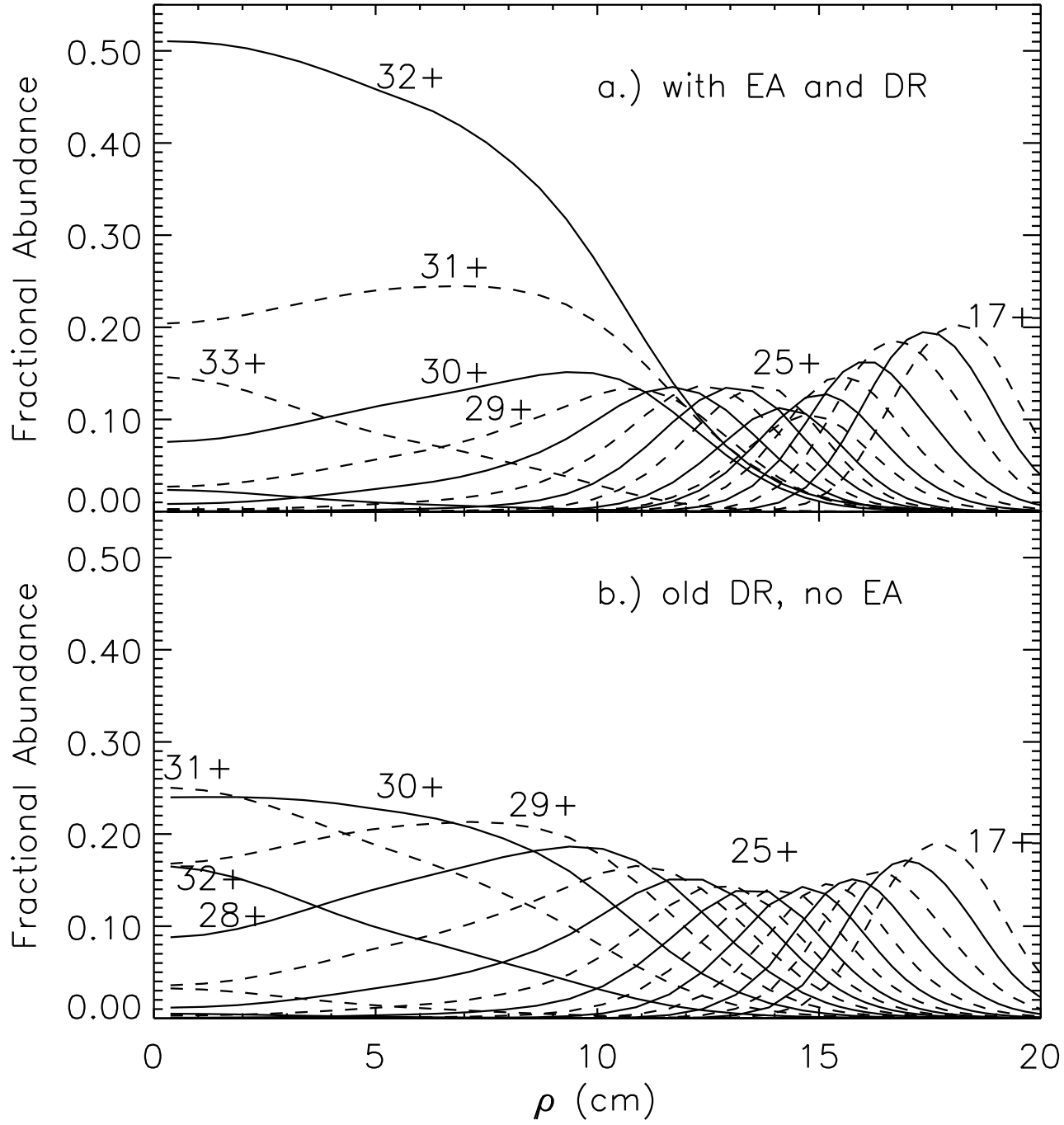
a.) with EA and DR
b.) old DR, no EA
Fractional Abundance
Fractional Abundance
0.50
0.40
0.30
0.20
0.10
0.00
0.50
0.40
0.30
0.20
0.10
0.00
32+
31+
33+
30+
29+
25+
17+
31+
30+
29+
25+
17+
32+
28+
0
5
10
15
20
ρ (cm)

Figure 10

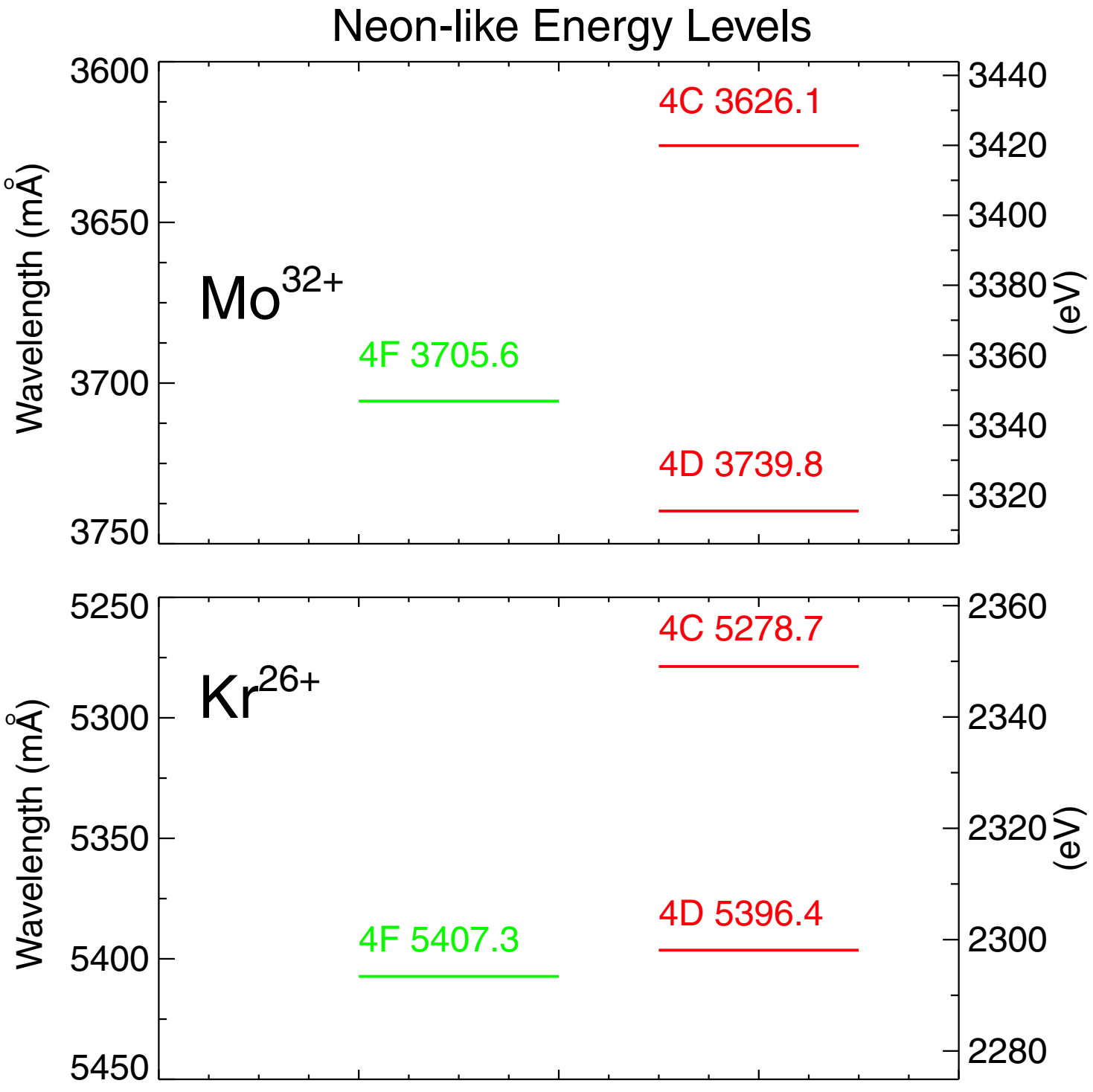
Neon-like Energy Levels
Mo32+
4C 3626.1
4F 3705.6
4D 3739.8
Wavelength (mÅ)
(eV)
3600
3650
3700
3750
3440
3420
3400
3380
3360
3340
3320
Kr26+
4C 5278.7
4F 5407.3
4D 5396.4
5250
5300
5350
5400
5450
2360
2340
2320
2300
2280

Figure 11

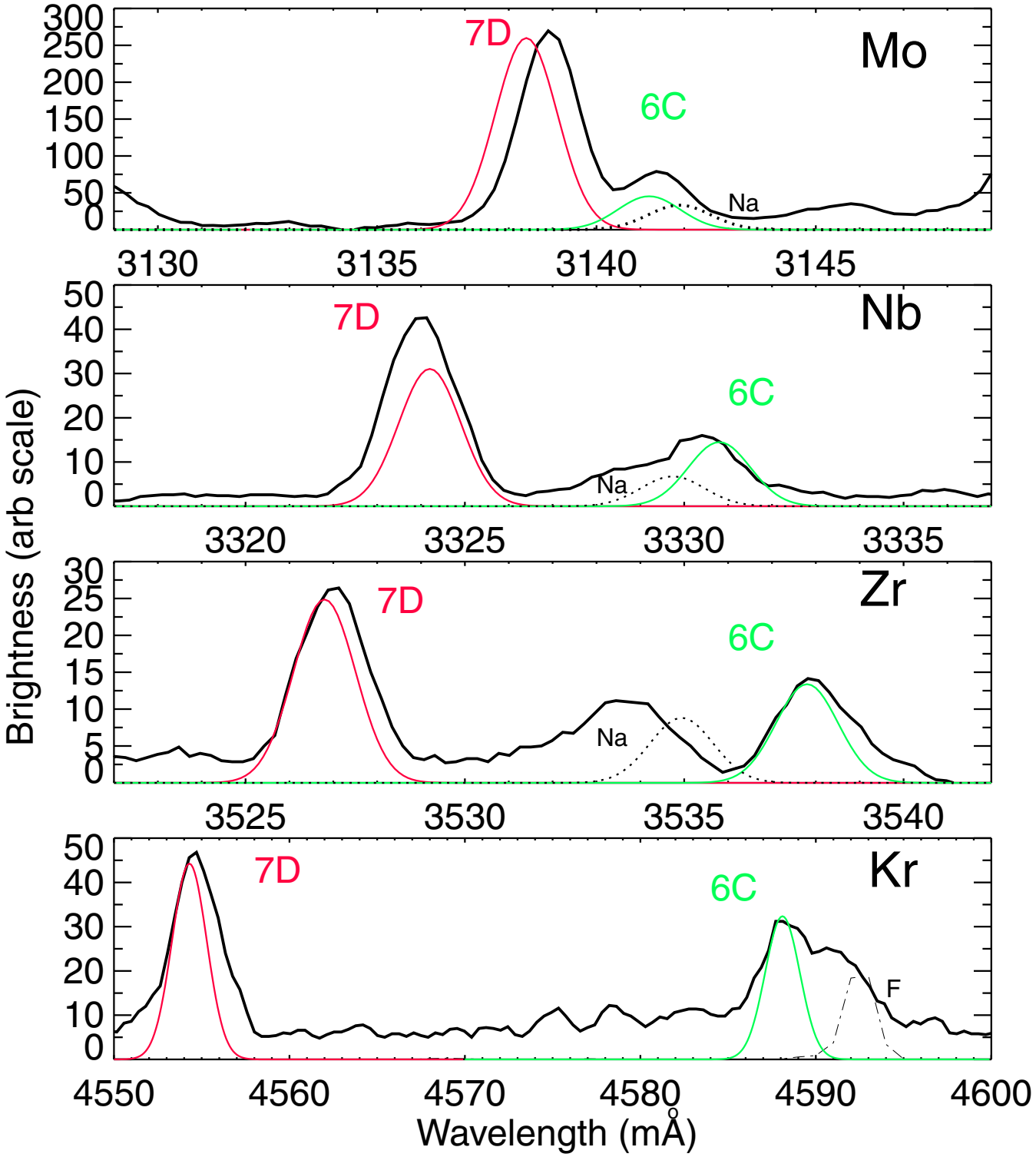
Mo
7D
6C
Na
Nb
7D
6C
Na
Zr
7D
6C
Na
Kr
7D
6C
F
Brightness (arb scale)
Wavelength (mÅ)

Figure 12

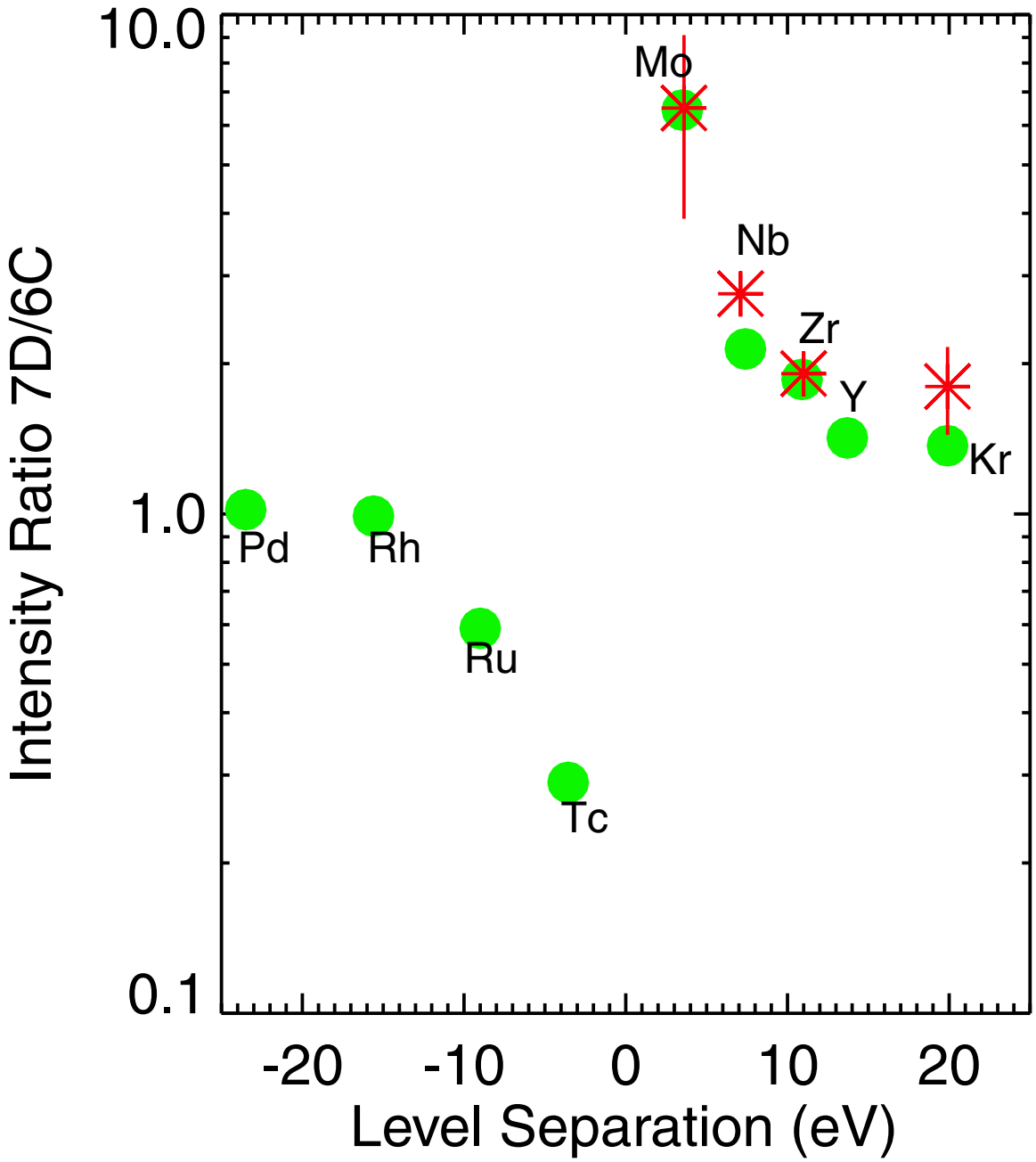
10.0
1.0
0.1
Intensity Ratio 7D/6C
Mo
Nb
Zr
Y
Kr
Pd
Rh
Ru
Tc
-20
-10
0
10
20
Level Separation (eV)

Figure 13

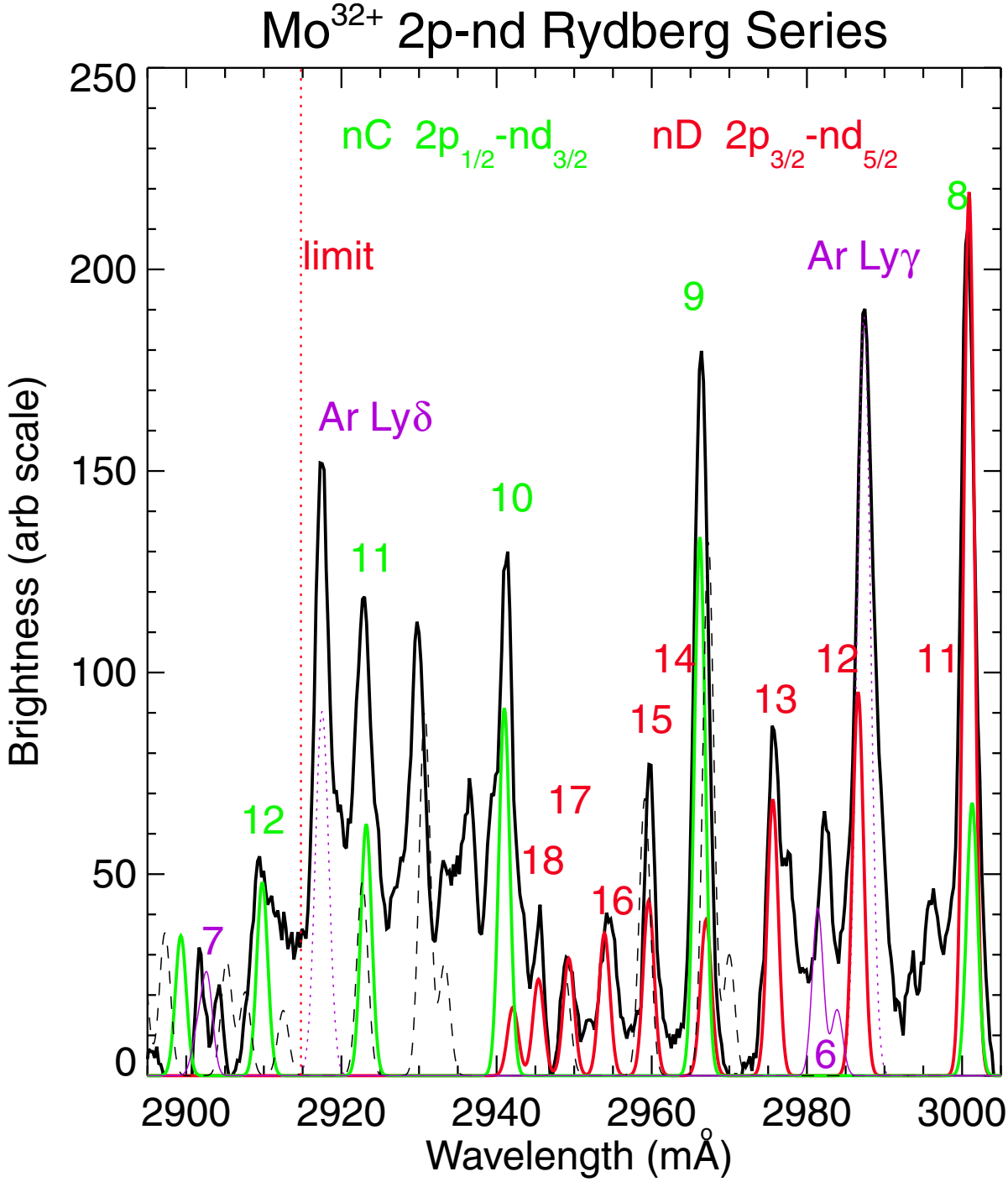
Mo32+ 2p-nd Rydberg Series
nC 2p1/2-nd3/2
nD 2p3/2-nd5/2
limit
Ar Lyδ
Ar Lyγ
Brightness (arb scale)
Wavelength (mÅ)
250
200
150
100
50
0
2900
2920
2940
2960
2980
3000
7
12
11
10
18
17
16
15
14
9
13
12
11
8
6

Figure 14